Optimization of an Air Core Dual Halbach Array Axial Flux Rim Drive for Electric Aircraft

Thomas Tallerico,[1] Jeffrey Chin,[2] and Zachary Cameron[3]
NASA Glenn Research Center, Cleveland, OH, 44135, U.S.A.

The anticipated development of the on-demand-mobility (ODM) market has accelerated the development of electric aircraft. Most proposed electric aircraft have propulsion systems that consist of fans directly driven by electric motors. The lower complexity of these propulsion systems opens the door to more custom propulsion system designs that are tailored to a given aircraft and its mission. This paper represents initial steps in the development of an electric propulsion system design code. A proof of concept version of the code is presented. The proof of concept version of the code is for the design of an axial flux rim driven propulsion system. NASA's all electric aircraft X-57, is used as a case study for this design code. The results of this case study are used to discuss the feasibility and potential benefits of using an axial flux rim driven propulsor on X-57. The final result of the case study shows a potential 4km increase in range over the current design.

I. Nomenclature

A_{coil} = stator coil cross sectional area
a = bearing moment center
B = magnetic flux density
B_{pk} = peak magnetic flux density
B_x = flux density in the tangential direction
B_z = flux density in the axial direction
C = basic dynamic bearing load rating
C_d = coefficient of drag
C_{d-2D} = 2D cascade drag coefficient
C_f = skin friction coefficient
C_{fill} = copper fill percentage
C_L = coefficient of lift
C_p = thermodynamic pressure coefficient
C_x = actual flow speed at fan entrance
C_{x2} = actual flow speed at fan exit
C_{y2} = tangential air velocity at fan exit
c = blade cord
dr = radial length of motor cross-sections
d_{wire} = diameter of litz wire strands
D = drag force
D_{bore} = bearing bore diameter
DF = diffusion factor
E_d = battery energy density
e = total aircraft battery to air efficiency
e_{bus} = bus efficiency
e_{fan1} = fan efficiency assumed
e_{fan2} = estimated actual fan efficiency
$e_{inverter}$ = inverter efficiency
e_{motor} = motor efficiency
F = force
h_b = blade height
H_{conv} = convective heat transfer coefficient
h_{fan} = fan enthalpy riser
I = current
I_i = mass moment of inertia about i axis
k = magnetic wave length
k_{air} = thermal conductivity of air
k_{copper} = thermal conductivity of copper
k_{epoxy} = thermal conductivity of epoxy
L = lift force
L_r = radial active motor length
$Loss_{bearing}$ = bearing losses
$Loss_{eddy}$ = eddy current loss
$Loss_{resistive}$ = resistive losses in stator
$Loss_{stator}$ = electrical stator losses
$Loss_{windage}$ = rotor windage losses
M = aircraft mass
M_{fan} = fan mass
M_g = gyroscopic moment vector
M_{motor} = motor mass
n_m = number of magnets per pole pair
OD_{fan} = fan outer diameter
OD_{motor} = motor outer diameter
P = bearing load
PR = pressure ratio
Pr = Prandlt number

[1] Aerospace Research Engineer, Rotating and Drive Systems
[2] Aerospace Research Engineer, Rotating and Drive Systems
[3] Aerospace Research Engineer, Rotating and Drive Systems

R_{phase}	=	electrical resistance single phase
RE_{air}	=	cooling flow Reynolds coefficient
Re_r	=	rotor tip Reynolds number
r_1	=	motor inner radius
r_2	=	motor outer radius
s	=	blade pitch
t_{ag}	=	airgap axial thickness
t_{coil}	=	coil/stator axial thickness
$t_{coil\ min}$	=	min stator coil thickness
t_g	=	axial distance between two rotors
t_m	=	axial thickness of the magnetic arrays
T_{air}	=	ambient air temperature
T_{stator}	=	stator thermal limit temperature
U	=	mean blade velocity
v	=	specific volume
V_{air}	=	flow velocity for cooling calculations
V_i	=	inlet velocity to fan
V_e	=	exit velocity from nozzle
ψ	=	stage loading factor
Vol_b	=	blade volume
w_{coil}	=	tangential width of a single coil
w_{magnet}	=	tangential width of a single magnet
x	=	tangential coordinate in motor cross-section
x_{st}	=	position of a coil in motor cross-section
z	=	axial coordinate in motor cross-section
ε	=	magnet rotor fill percentage
α_2	=	flow exit angle relative to stator
β_m	=	mean flow angle
β_1	=	flow angle relative to compressor rotor
β_2	=	flow angle relative to compressor stator
σ_{copper}	=	electrical conductivity of copper
γ	=	ratio of specific heats
ρ_{air}	=	density of air
μ_{air}	=	dynamic viscosity of air
μ_f	=	bearing coefficient of friction
ω	=	angular velocity

II. Introduction

The anticipated development of the on-demand-mobility (ODM) market has accelerated the development of electric aircraft. Most electric aircraft currently proposed use fans directly driven by electric motors. The low complexity of these systems, especially when compared to a turboprop engine, opens the door for more customized propulsion system designs. These propulsion system designs can be optimized to maximize the performance of a specific aircraft.

This paper represents initial steps in the development of an electric aircraft propulsion system design code. The aim of the code development is to produce a tool for optimization of electric propulsion systems for any given aircraft and its mission. In this paper, an initial proof of concept version of the code is presented. This version of the code is for the design of an air core axial flux rim driven fan. The code combines low fidelity motor, fan, and aircraft models to develop a preliminary electric propulsion system design for an aircraft.

Rim driven electric fans were chosen for the initial code development because they enable higher tip speeds for the electric motor than their hub driven counterparts. High tip speed is an indicator of either high rpms or large motor radii. At a set power, higher rpms reduce the torque/force the motor has to produce, thereby reducing the required current and/or the electromagnetic mass. Large motor radii put the electric motor at a mechanical advantage also reducing the force the motor has to produce and leading to the same possible improvements. There are mechanical limits to how high motor tip speed can be driven. At very high tip speeds centripetal loading on the rotor requires heavy mechanical solutions and windage losses become significant [Ref. 1].

To demonstrate the code, a case study of a propulsion system design for NASA's X-57 all electric aircraft [Figure 1] has been performed. In this paper, the code will be discussed in the context of the case study and then the results of the case study will be discussed. Lastly, some validation of the case study results is included.

Figure 1 Rendering of NASA's X-57 Electric Aircraft Mod 2 Configuration

III. Design Code Models

The version of the design code presented in this paper combines low fidelity motor, fan, and electric aircraft range models to tailor a propulsion system design to a given aircraft. In the following sections the low fidelity models will be discussed in the context of the axial flux air core dual rotor rim drive for X-57 design case study.

The motor model in this paper is for dual rotor halbach array air core axial flux motors. Because this motor topology is air core and halbach arrays are used on the rotor, there is no nonlinearity in the system and simple electromagnetic equations can be used to calculate motor performance. The air core also decreases the motor's electrical frequency dependent losses. This low loss dependence on electrical frequency, makes these motors practical for rim driven applications as they can use higher pole counts than their iron core counter parts. Additionally, the axial flux topology of the motor provides better thermal paths for heat rejection from the stator, because the copper windings span from the outer radius to the inner radius of the stator.

There are some drawbacks to the use of axial flux motors for rim drives. Unlike their radial flux counterparts, increasing axial flux motor's stack length directly increases the radius and tip speed of the machine. Larger machine radii requires larger shells/housings around the propulsion system increasing both the drag and mass of the propulsion system. Additionally if the ideal fan design has a tip speed in the .55 to .7 Mach range, increases to motor stack length will result in large increases in windage losses on the motor rotors. A balance between fan diameter, fan tip speed, and motor stack length has to be achieved to produce a high performance axial flux rim driven fan.

The fan model used in the code is for ducted fans. It combines thermodynamic analysis and blade element theory to produce preliminary fan designs. Ducted fans generally tend to have lower mass flow rates than propellers because the mass of the ducting increases directly with mass flow. They also typically have lower efficiency relative to propellers at low flight speeds.

The aircraft model is the Breguet range equation for electric aircraft [Ref 2]. This model is used for its simplicity and because it is a good indicator of X-57's performance as its mission profile is dominated by cruise. Range is used as the metric for aircraft performance. Any range improvement could easily be traded for more payload or reduced battery mass at a constant range.

A. Motor Model

The motor model used in this version of the design code is for a dual rotor air core axial flux machine. Table 1 lists the assumptions made about the motor topology and the material properties used in the code.

The electrical frequency of the machine is limited to 1 kHz to make the machine compatible with current inverter technology. Because this machine topology has no iron, the only electrical frequency dependent losses are eddy current losses in the stator windings. These losses can be limited through the use of twisted litz wire with a small strand gage. The design code thereby favors higher electrical frequencies than would be realistic for current inverter technology to drive efficiently.

The number of motor stacks refers to how many sets of rotors and coils the machine has. In this paper it is assumed that stacks share a rotor. For one motor stack, there are two rotors and one stator. For two motor stacks, there are three rotors and two stators. This rotor sharing allows for some mass reduction for multiple stacks.

The machine stator is assumed to have three phases with three slots per rotor pole pair. Concentrated windings with two side by side layers per slot are assumed for simplicity. The windings are assumed to have 50% copper fill. A highly thermally conductive, electrically insulating epoxy is assumed to make up the other 50% of each coil. The operating temperature of the stator is set to 400 K and the copper resistivity is set based on this temperature. The wire is assumed to be litz wire with 36 AWG strands.

Outer rotors are assumed to be permanent magnet rotors with Halbach arrays and no back iron. Inner rotors are assumed to be normal magnetic north south arrays with no back iron. The magnets are assumed to be rectangular. The number of magnets per pole is set to 8. A carbon fiber hoop is assumed to hold the centripetal loading of the magnets.

In the following sections, the model for motor torque will be discussed, followed by a description of the loss and thermal models used.

Table 1 Motor Model Assumption

Motor	
Topology	Dual Rotor Axial Flux
Core	Air Core
Max Electrical Frequency	1kHz
Airgaps	1 mm
Number of Motor Stacks	1 or 2
Stator	
Number of Phases	3
Slots/Pole	1.50
Winding Type	Concentrated
Layers Per slot	2.00
Layout	Side-by-Side
Max Allowable Temperature	400 K
Conductor Material	Copper
Copper Fill	50%
Copper Electrical Resistivity	2.46e-8 (Ohm*m)
Copper Thermal Conductivity	386 (W/(m*K))
Copper Density	8960 (kg/m^3)
Wire	Litz Wire with 36AWG Strands
Matrix Material	Resin Epoxy
Epoxy Thermal Conductivity	1 (W/(m*K))
Epoxy Density	1225 (kg/m^3)
Rotors	
Topology	Permanent Magnet Halbach Array
Gaps Between Adjacent Magnets	(1mm)
Magnets	
Material	NdFeB grade 45SH
Shape	Rectangular
Remnant Flux Density (Br)	1.35 (T)
Density	7500 (kg/m^3)
Max Temp	145(C)
Magnet Retaining Hoop	
Material	Carbon Fiber
Max Allowable Stress	600 (MPa)

1. Electromagnetic Torque Calculation

The model used to predict torque is based on the low fidelity electromagnetic model for dual rotor axial flux motors presented in reference 3. The model maps radial cross sections of a single pole pair of the motor to an x-z plane as shown in Figure 2 below.

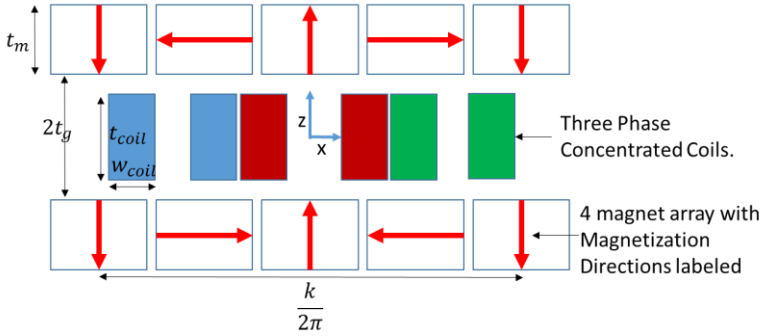

Figure 2 Example of an axial flux motor radial cross section mapped to an x-z plane

The code calculates the torque produced at each radial cross section using the equation for force on a current carrying wire in a magnetic field:

$$F = B \times I d_r \tag{1}$$

Here F is the force on the wire, B is the magnetic field, $\times$ is the cross product, I is the current in the wire, and d_r is the radial length of the radial cross section. In this model the B field in the equation is assumed to only come from the permanent magnet rotors. Any field produced by the coils is neglected. Because the machine has no iron, superposition of fields holds and neglecting the field produced by the coils has no effect on the accuracy of the force calculation. The B field created by the rotor is calculated for a given radial cross section of the motor using the analytic equations for the field between two linear Halbach arrays [Ref 4]:

$$B_x = 2B_r e^{-k*t_g}(1 - e^{-k*t_m}) \frac{\sin\left(\frac{\epsilon\pi}{n_m}\right)}{\frac{\pi}{n_m}} \sin(kx)\sinh(kz) \tag{2}$$

$$B_z = 2B_r e^{-k*t_g}(1 - e^{-k*t_m}) \frac{\sin\left(\frac{\epsilon\pi}{n_m}\right)}{\frac{\pi}{n_m}} \cos(kx)\cosh(kz) \tag{3}$$

Here B_z is the magnetic field in the motor's axial direction, B_x is the field in the motor's tangential direction, k is the wave number of the magnetic field produced by the rotors at a given radial cross section, t_g is half the axial distance between the two rotors, t_m is the magnet axial thickness, ϵ is the percent of the tangential arc length the magnets on each rotor cover at a given radial cross section, n_m is the number of magnets that are used to form each pole pair of the rotor, x is the position in the tangential direction, and z is the position in the axial direction. Figure 2 shows how the x-z coordinate frame is defined for each radial cross section of the motor. The radial portion of the magnetic field is neglected in this model.

The motor design code uses ten radial cross sections. At each radial cross section it defines the stator coil positions and computes the average axial flux density in each coil cross section using equation 2. The code then computes the force on each cross section of the coils using equation 1 so that

$$F_{coil\ dr} = dr * \frac{2IB_rC_{fill}}{w_{coil} * t_{coil}} \int_{x_{st}}^{x_{st}+w_{coil}} \int_{-\frac{t_{coil}}{2}}^{\frac{t_{coil}}{2}} B_z \, dz \, dx \tag{4}$$

Here $F_{coil\ dr}$ is the x direction force on a given coil at a given motor cross section, dr is the radial length of the cross-section, I is the current in the coil, C_{fill} is the copper fill percentage, w_{coil} is the coil width in the x direction, t_{coil} is the coil thickness in the z direction, and x_{st} defines the position of each coil in the x direction. Torque for the motor

is then computed by summing all ten $F_{coil\ dr}$ times their radial cross section position and multiplying by the number of pole pairs in the machine.

2. Eddy Current Loss in Windings

The eddy current in the windings are predicted using the equation for eddy current loss in round conductors found in reference 5. In terms of the variables used in the motor design code it is written

$$Loss_{eddy} = 6N_P \frac{\pi^2}{4} \sigma_{copper} * f^2 * d_{wire}^2 * L_r w_{coil} t_{coil} * B_{pk}^2 \quad (5)$$

Here $Loss_{eddy}$ is the total eddy current loss for the machine, N_P is the number of pole pairs in the machine, σ_{copper} is the electrical conductivity of copper, f is the operating electrical frequency of the machine, d_{wire} is the diameter of a single litz wire strand, L_r is the radial length of the active section of the machine, and B_{pk} is the max flux density that occurs in the stator windings. B_{pk} is calculated using equations 2 and 3.

This loss is the only electrical frequency dependent loss that occurs in the machine. Through the use of small wire strands in the litz wire it can be minimized so that very high electrical frequencies can be used in the machine.

3. Windage Loss on Rotors

The higher motor tip speed achieved by using a rim drive configuration improves the electrical efficiency of the machine; however, windage losses on the rotors can become significant. In this code the windage loss on the motor's rotors is approximated using the equations for windage power loss on enclosed rotating disks found in references 6 and 7. The power loss per rotor is defined by

$$Loss_{windage} = .5 C_f \rho_{air} \omega^3 (r_2^5 - r_1^5) \quad (6)$$

Here $Loss_{windage}$ is the windage power loss on a given rotor, C_f is the skin friction coefficient, ρ_{air} is the density of air, ω is the rotational speed of the rotors, r_2 is the outer radius of the rotor including its carbon fiber retaining hoop, and r_1 is the inner radius of the rotor. In the flow regime all rotor designs in this paper fall into, the skin friction coefficient is defined by

$$C_f = \frac{.08}{\left(\frac{t_{ag}}{r_1}\right)^{.167} Re_r^{.25}} \quad (7)$$

Here t_{ag} is the axial thickness of the motor airgaps, and Re_r is the tip Reynolds number given by

$$Re_r = \frac{\rho_{air} \omega r_2^2}{\mu} \quad (8)$$

Here μ is the dynamic viscosity of air.

In the design of axial flux rim driven fans, windage loss is a major driver of the final geometry. It imposes limits on both the fan and motor tip speeds. Because of this loss mechanism, for a given rotational speed the fan diameter and the radial length of the motor have to be balanced to achieve an efficient propulsion system.

4. Bearing Loss

Bearing losses are accounted for based on equations found in references 8 and the SKF catalog [Ref 9]. Bearing loss is defined by

$$Loss_{bearing} = M * \omega = .5 \mu_f * D_{bore} * F_{bearing} * \omega \quad (9)$$

Here $Loss_{bearing}$ is the bearing loss at a given rotational speed, M is the moment the bearing frictional force creates, μ_f is the bearing friction coefficient, D_{bore} is the bearing bore diameter, and $F_{bearing}$ is the total force on the bearing.

In the case study presented in this paper, the fan and motor are assumed to be supported by a double row angular contact bearing with a 25mm bore diameter. The validity of this bearing selection will be discussed in section VI C. $F_{bearing}$ is assumed to be the sum of the thrust produced by the fan and the weight of the rotors and fan. μ_f is set to .0024 based on the friction coefficient recommended for double row angular contact bearings in references 9.

5. Resistive Losses

Resistive losses are calculated by

$$Loss_{resistive} = 3 * R_{phase} * \left(\frac{I_{pk}}{\sqrt{2}}\right)^2 \quad (10)$$

Here I_{pk} is the peak current per coil and R_{phase} is given by

$$R_{phase} = \frac{N_{coil} * l_{coil}}{\sigma_{copper} A_{coil} C_{fill}} \quad (11)$$

Here N_{coil} is the number of coils per phase, l_{coil} is the length of each coil including end turns, and A_{coil} is the cross-sectional area of a single coil.

6. Motor Thermal Model

For the propulsion system topology explored using the design code in this paper it is assumed that the stator is cooled with the prop wash at its inner radius. Because the motor topology being explored in this paper has copper windings providing a highly thermally conductive path from the stator's outer radius to its inner radius, the stator is assumed to have a uniform temperature. This temperature is set to 400 Kelvin in order to provide temperature margin assuming the winding insulation is rated to 420 Kelvin.

A flat plate convection model [Ref 10] is used at the inner radius to set a min stator thickness based on the losses in the stator. Because of the large radius of the machine this is a reasonable assumption. The minimum stator coil thickness is defined by

$$t_{coil\ min} = \left(\frac{Loss_{stator}}{2\pi H_{conv} r_1 (T_{stator} - T_{ambient})}\right)^2 \quad (12)$$

Here $t_{coil\ min}$ is the min stator thickness required to keep the stator from overheating, $Loss_{stator}$ is the sum of the resistive and eddy current losses on the stator, H_{conv} is a coefficient calculated based on a flat plate convection model, T_{stator} is the assumed temperature of the stator, and $T_{ambient}$ is the temperature of the atmosphere. H_{conv} is given by

$$H_{conv} = .644 * k_{air} Pr_{air}^{\frac{1}{3}} Re_{air}^{.5} \quad (13)$$

Here k_{air} is the thermal conductivity of air, Pr_{air} is the Prandlt number, and RE_{air} is a Reynolds number coefficient given by

$$RE_{air} = \frac{\rho_{air} V_{air}}{\mu_{air}} \quad (14)$$

Here ρ_{air} is the density of air, V_{air} is the air axial velocity, and μ_{air} is the dynamic viscosity of air. V_{air} is assumed to be aircraft cruise speed for the model presented in this paper. All other air properties are evaluated at aircraft cruise altitude.

B. Ducted Fan Model

Fan design is carried out through a combination of low fidelity thermodynamic cycle analysis and fan blade analysis. Assumptions made in this model are in Table 2.

All ambient/cruise air conditions are based on an altitude of 2400m. The cruise speed matches that of X-57. Compressor pressure ratios and efficiencies were set based on preliminary model results. The thrust per propulsor was set equal to half the drag on X-57 in cruise.

The fan blade model assumes there is no initial swirl to the incoming air and the flow is purely perpendicular to the fan. The coefficient of lift values are based on recommendations for ducted fans found in reference 13. The blade cord was set to 5cm (2 in) because the model's mass estimate heavily favored smaller blade sizes. 5 cm was determined to be a reasonable value for realistic blade designs. The pitch-to-cord ratio was kept between 0.9 and 1.2 per recommendations in references 11 and 13. The Diffusion Factor, Stage Loading Factor, and Hub-to-Tip Ratio were the 3 inputs along with the thermodynamic results to the blade analysis. The values for Stage Loading and Diffusion Factor are based on recommendations in reference 11. The assumed Hub-to-Tip Ratio was assumed to be 0.3, but 0.15 and 0.45 where included to create some spread in the results.

Table 2 Fan model Assumptions

Thermodynamic Analysis Assumptions	
Cp	1005 (J/(kg*K))
γ	1.401
Cruise Speed	74.475(m/s)
Cruise Mach Number	0.255
Cruise Speed of Sound	331 (m/s)
Cruise Temperature	272.55 (K)
Cruise Pressure	75.5 (kPa)
Air Density	1.004 (Kg/m^3)
Compressor Pressure Ratio	1.01-1.15
Compressor Efficiency	70-94 (%)
Outlet Efficiency	98 (%)
Outlet Exit Conditions	75.5 (kPa)
Thrust	575 (N)
Fan Blade Model Assumptions	
Incoming Flow Direction	Perpendicular to fan
Number of Stages	1
Coefficient of Lift at Hub	0.9
Coefficient of Lift at Tip	0.6
Blade Chord	.05 (m)
Pitch to Chord Ratio	.9-1.2
Stage Loading Factor	.35-.55
Diffusion Factor	.35-.55
Hub to Tip Ratio	.15,.30,.45
Fan Mass Estimate Assumptions	
Blade Material	Titanium
Blade Disk Material	Titanium
Outer Shell Material	Aluminum
Outer Shell Thickness	3 (mm)
Flow Straightener Mass	Equal to Fan Mass

1. Thermodynamic Model

Thermodynamic analysis is performed using 1D thermodynamic equations for an inlet, compressor, and outlet. The equations were taken from references 11 and 12. For the version of the code presented here, the inlet is neglected due to the low assumed cruise speed of X-57. The compressor inlet conditions and other assumptions for the thermodynamic model are listed in Table 2.

Fan inlet total pressure and total temperature are calculated from the cruise conditions using isentropic flow equations. An adiabatic efficiency and a pressure ratio are assumed for the fan. Fan work per unit mass flow is calculated based on the isentropic enthalpy rise created by the pressure ratio. Actual enthalpy rise is calculated using the assumed efficiency. Fan outlet total temperature and pressure are calculated based on the actual enthalpy rise.

For the nozzle, a 98% efficiency is assumed. The outlet enthalpy is calculated using this efficiency and the fan exit enthalpy. The outlet exit total temperature and pressure are calculated based on the nozzle exit enthalpy. Nozzle exit pressure is calculated by using the difference between the total pressure and the ambient pressure. Thrust per nozzle exit area is then calculated using.

$$\frac{Thrust}{A_e} = \rho_{air} V_e * (V_e - V_i) \tag{15}$$

Here V_e is nozzle exit velocity, V_i is cruises speed, and A_e is the nozzle exit area. Nozzle exit area is then scaled to achieve the required thrust.

These calculations are carried out across all possible combinations of the assumed compressor pressure ratio and efficiency. The following fan blade analysis is used to check which assumed efficiency and pressure ratios combinations are valid.

2. Low Fidelity Fan Blade Analysis

Low fidelity fan blade analysis takes in all of the results of the thermodynamic analysis and uses isolated airfoil and blade element theory to determine which thermodynamic analysis results are valid for a given set of fan design parameters (Diffusion Factor, Stage Loading, and Hub-to-Tip Ratio). It determines which results are valid by recalculating the compressor efficiency for each thermodynamic result and comparing it to the efficiency that was assumed in the thermodynamic model. All calculations for the fan blade analysis are done at the average fan radius. The assumptions used in the version of the code presented here are in Table 2. The source for all the below equations is reference 11 unless otherwise noted.

For each output of the thermodynamic model, the blade analysis is performed for all possible assumed combinations of fan hub to tip ratio, stage loading factor, and diffusion factor. The fan's inner, outer, and mean radii are calculated using the assumed hub to tip ratio for the fan. The tangential velocity of the fan blades at the mean radius is calculated using the stage loading factor by

$$\psi = \frac{\Delta h_{fan}}{U^2} \tag{16}$$

Here ψ is the stage loading factor, Δh_{fan} is the adiabatic enthalpy change created by the fan in the thermodynamic model, and U is the fan tangential velocity at the mean radius.

The air entering the fan is assumed to have a velocity perpendicular to the fan and equal to the aircraft cruise speed. This assumption allows the angle of the airflow relative to the fan's air foils to be calculated by

$$\tan(\beta_1) = \frac{U}{V_i} \tag{17}$$

Here β_1 is the airflow entrance angle relative to the fan's airfoils. The assumed stage loading factor is used to calculate the airflow exit angle relative to the fan's airfoils using

$$\psi = \frac{V_i}{U}(\tan(\beta_1) - \tan(\beta_2)) \tag{18}$$

Here β_2 is the airflow exit angle relative to the fan's airfoils. The airflows exit angle relative to the flow straightener airfoils is calculated using

$$\tan(\alpha_2) = (\tan(\beta_1) - \tan(\beta_2)) = \psi * \frac{U}{V_i} \tag{19}$$

Here α_2 is the airflow exit angle relative to the flow straighteners. These three angles and the assumed diffusion factor are used to calculate the blade pitch using

$$DF = \left(1 - \frac{\sqrt{1 + \tan(\beta_2)^2}}{\sqrt{1 + \tan(\beta_1)^2}}\right) + \frac{s}{2c}\frac{\tan(\alpha_2)}{\sqrt{1 + \tan(\beta_1)^2}} \tag{20}$$

Here DF is the assumed diffusion factor, s is the blade pitch, and c is the assumed blade chord. Fan designs with pitch-to-chord ratios outside the assumed allowable range are disregarded.

The coefficient of lift for the blades was assumed to be 0.9 at the hub and 0.6 at the blade tips per recommendations found in reference 14. The coefficient of lift at the mean radius was estimated using a linear interpolation between these points. Based on reference 13, coefficient of drag for the blades was defined as

$$C_D = C_{d-2D} + .02\frac{s}{h_B} + .018{C_L}^2 \tag{21}$$

Here h_B is the blade height, C_L is the assumed coefficient of lift, and C_{d-2D} is the 2D cascade blade drag defined by

$$C_{d-2D} = \frac{2 * \frac{s}{c}\tan(\alpha_2)\cos(\beta_m) - C_L}{\tan(\beta_m)} \tag{22}$$

Here β_m is the mean flow velocity relative to the airfoils defined by

$$2 * \tan(\beta_m) = (\tan(\beta_1) + \tan(\beta_2)) \tag{23}$$

Fan efficiency can then be calculated by

$$e_{fan} = \frac{V_i}{U}\tan\left(\beta_m - \text{atan}(\frac{C_D}{C_L})\right) + \tan(\alpha_2)\frac{V_i}{2U} \tag{24}$$

Here e_{fan} is the ducted fan's efficiency. In each case, e_{fan} is compared to the assumed efficiency in the thermodynamic analysis. If the two efficiencies values are within 0.1% the thermodynamic result is assumed to be valid. For each set of fan blade analysis parameters multiple thermodynamic analysis results are valid. Only the result with the highest efficiency is kept.

3. Fan and Duct Mass Estimate

Fan blade mass is calculated using the method described in reference 15. It defines a rough estimate of blade volume as

$$Vol_B = .055 * h_B * c^2 \tag{25}$$

Where Vol_B is the volume of a single rotor blade. In this paper the blades are assumed to be made out of titanium. The flow straighteners are assumed to have equal mass to the rotor blades. Additionally it is assumed that the rotor is connected to the bearings using a titanium disk of thickness equal to the blade chord.

The mass of the shell around the fan, motor and nozzle is estimated by two 3mm thick cylinders of aluminum. The two cylinders are meant to represent a hollow casing around the propulsor. They have the diameters of the inlet and the motor respectively. The inner cylinder estimates the inner duct wall mass and the outer cylinder estimates the outer casing.

C. Aircraft Model

For this initial design electric propulsion system code development and the case study presented in this paper, the Breguet range equation [Ref 2] is used to evaluate the effect different propulsion system designs have on electric aircraft performance. The equation defines the range of an electric aircraft as

$$Range = e\frac{L}{D}\frac{E_{density}\, m_{battery}}{m_{total}} \tag{26}$$

Here e is the aircraft efficiency, L is the aircraft lift coefficient, D is the aircraft drag coefficient, $E_{density}$ is the battery energy density, $m_{battery}$ is the mass of the battery, m_{total} is the total mass of the aircraft. e in this paper is defined as

$$e = e_{fan}e_{motor}e_{inverter}e_{Bus} \tag{27}$$

Here $e_{component}$ is the efficiency of each component.

For the case study in this paper the values used to model the X-57 mod 2 baseline configuration [Ref. 16, 17, 18, and 19] are listed in the Table 3 below.

Table 3 Breguet Range Equation Modeling Parameters

Parameters Used to Model X-57	
Lift at Cruise	**13351 (N)**
Drag at Cruise	**1147.4 (N)**
Battery Energy Density	**810000 (W*s/kg)**
Total Mass	**1360 (kg)**
Fuselage	509.4 (kg)
Wing	85.411 (kg)
Motor	27.2 (kg)
Nacelle	26.2 (kg)
Batteries	345.6 (kg)
Fan	14 (kg)
Inverter	7 (kg)
Total Efficiency [e]	**75.80 (%)**
Fan	82.8 (%)
Motor	95 (%)
Inverter	96 (%)
Bus	99 (%)
Estimated Range	**182.3 (km)**

When the values in Table 3 are used the Breguet range equation predicts a range of 182.3 kilometers for X-57. The design code in this paper evaluates the performance of different propulsion system designs by updating e_{fan}, e_{motor}, m_{fan}, m_{motor}, and $m_{naucelle}$. Drag is left constant because the aerodynamic modeling required to update this term is outside the scope of this paper.

IV. Design Methodology

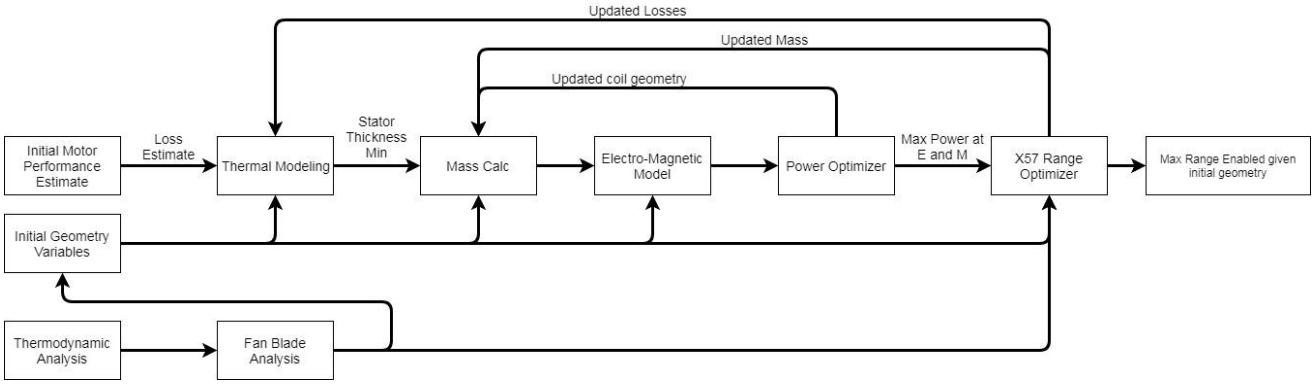

Figure 3 Flow Diagram of Propulsion System Design Methodology

A flow diagram for the electric propulsion system design code is shown in Figure 3. The design process starts by running the thermodynamic model to size fans for all the assumed compressor pressure ratios and efficiencies. The fan design code then performs parametric sweeps on the Stage Loading Factor, Diffusion Factor, and Hub-to-Tip ratio. The highest efficiency fan design that is found to be valid for each parameter set is kept. The fan designs are then down selected based on mass and efficiency. Once a fan design is selected, its parameters are fed into the motor design code. The fan design defines the rotational speed of the propulsion system, the inner radius of the motor, and the

required shaft power. The motor's pole count is set to make the electrical frequency 1 kHz. A starting electromagnetic mass and total loss for the motor is then fed into the motor design code.

The motor design code starts by calculating the thickness of the carbon fiber retaining hoop required based on the radial length of the magnets. Windage and bearing losses are calculated and subtracted from the total motor loss to define the allowable stator losses. The minimum stator thickness is then calculated using the thermal model. Stator winding width is set to a minimum value. The mass of the stator coils is then calculated and subtracted from the total motor mass to define the mass and thickness of the magnets. Stator winding eddy current losses are then calculated and subtracted from the stator loss to calculate the allowable resistive losses. The resistive loss model is used to calculate the stator current from the allowable losses. The torque model uses this current along with the coil and magnet geometries to calculate the torque for this initial design and set the base power.

The motor design code reruns the torque and stator loss calculations twice, once increasing the coil thickness by 1% and once increasing the coil width by 1%. Magnet geometry is updated each time based on the increased coil mass. The change that results in the highest increase in power over the base power is kept and the base power is updated accordingly. The torque and stator loss calculations are then repeated updating the motor geometry and base power until neither a change in coil width or coil thickness produces a higher power than the base power.

The range optimizer takes in the motor base power, motor mass, motor loss level, fan efficiency, fan required shaft power, and fan mass. If motor base power does not exceed the sum of the fan required shaft power, the windage losses, the eddy current losses, and the bearing losses, the allowable losses for the motor are increased by 1% and the motor design code is rerun. If the motor base power does exceed the sum of the fan required shaft power, the windage losses, the eddy current losses, and the bearing losses, a base range value is calculated given the input motor and fan information. The range optimizer then calculates the range increases for both a 1% reduction in motor mass and a 1% improvement in motor losses. The motor design code is then rerun with the change that produces the greatest increase in range. The new motor design info is then fed into the range optimizer and the process is repeated until the motor base power is within 1% of the sum of the fan required shaft power, the windage losses, the eddy current losses, and the bearing losses.

Parametric sweeps are then performed updating the number of motor stacks and the motor's active length. The design from these sweeps that results in the largest aircraft range is then selected.

V. Case Study Results

All assumptions made for the case study can be found in the above Tables and the model descriptions. In the below sections the results of the parametric sweeps for both the fan design code the motor design will be discussed. Overall aircraft performance improvements are discussed with the motor design sweeps.

A. Fan Design Code Parametric Sweeps

Parametric sweeps were performed on the fan stage loading factor, diffusion factor, and hub to tip ratio. As noted previously the fan design code only outputs the fan design with the maximum efficiency for each set of parameters. For all parameter sets used in this case study this always resulted in a fan efficiency of around 80% and fan pressure ratios of about 1.025. The following sections will discuss the trends with respect to overall propulsor efficiency and fan mass. Results that didn't have a pitch-to-chord ratio between .9 and 1.3 have been omitted.

1. Results of Fan Design Parametric Sweeps

a. Efficiency

For the majority of fan designs without a nozzle pressure ratio output by the code, efficiency was in-between 78 and 81 percent. The below plots in Figure 4 show all the results for the parametric sweeps with respect to efficiency.

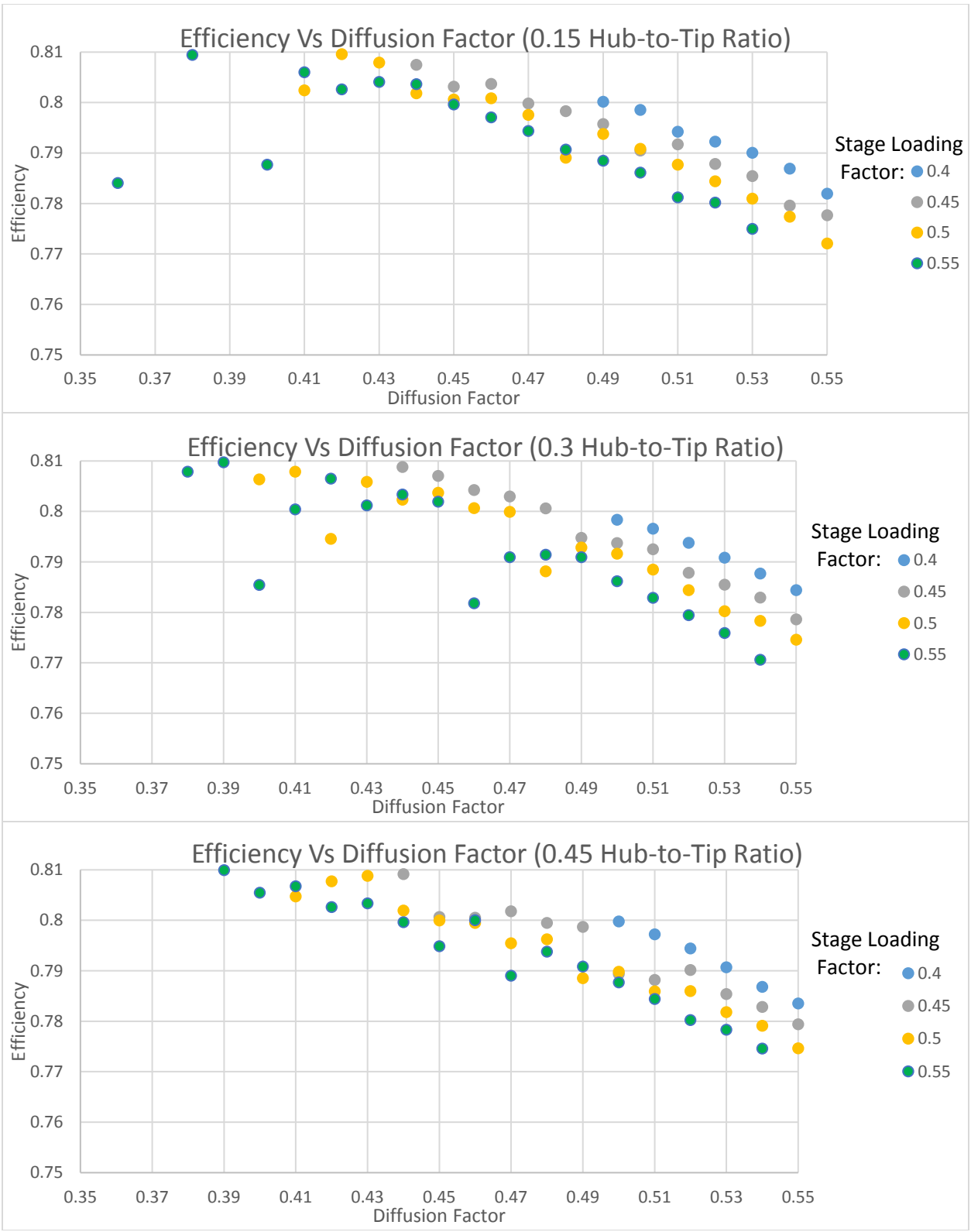

Figure 4 Fan Efficiency Vs Diffusion Factor for all hub to tip ratio and stage loading factor used in the case study

Increasing Stage Loading or Diffusion Factor always decreases fan efficiency. High Diffusion Factors or Stage Loading Factors correspond to higher pressure ratios and lower mass flow. Because exit velocity and thrust trend with the square root of pressure rise lower pressure rises and more mass flow is more efficient.

Hub-to-Tip Ratio also increased efficiency slightly, but it may have been a consequence of the linear interpolation used to determine the coefficient of lift for the fan blades at the mean radius. As Hub-to-Tip Ratio increases the mean radius moves closer to the hub and thereby has a higher coefficient of lift.

b. Mass

The plots in Figure 5 show the masses for all parameter combinations.

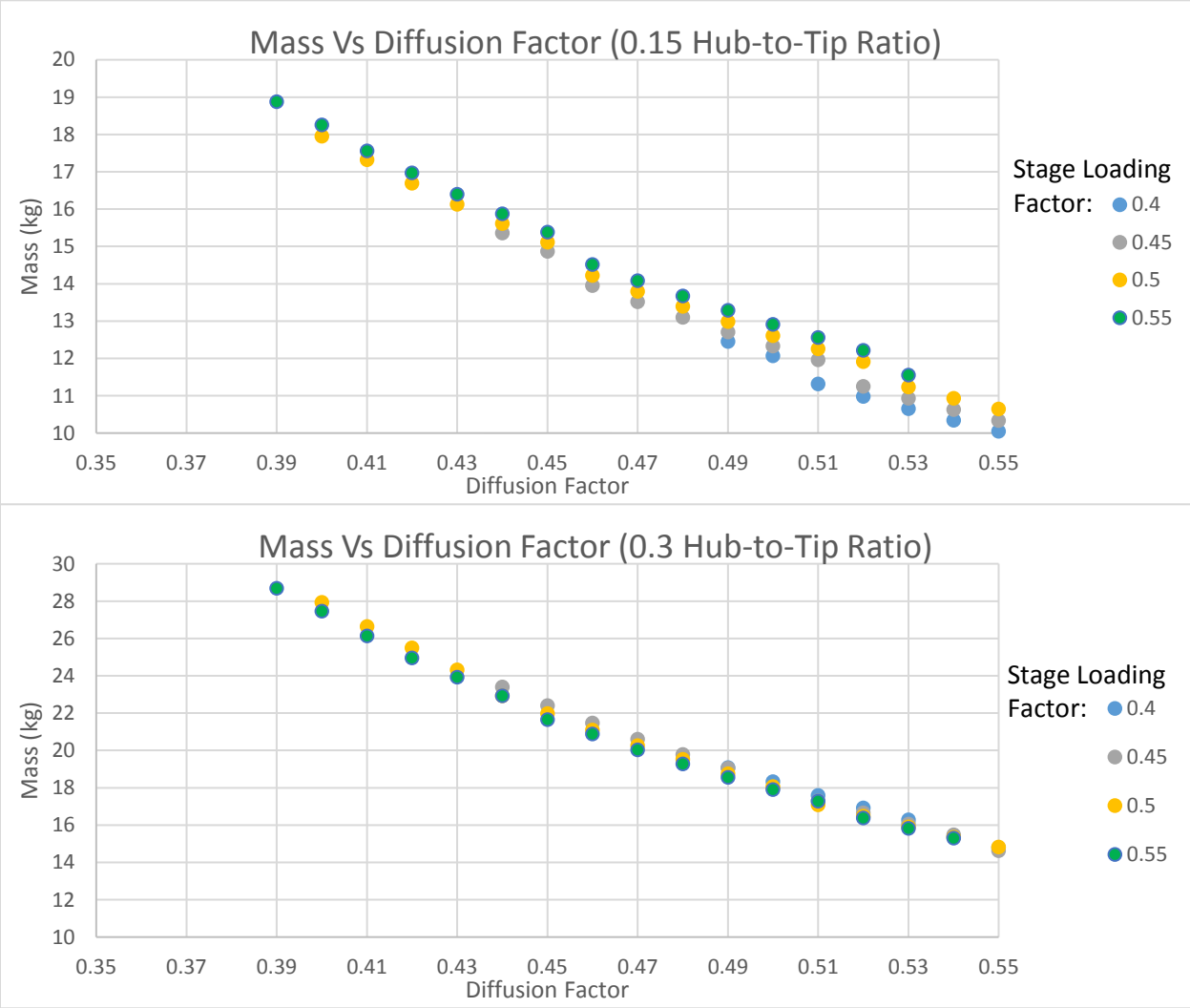

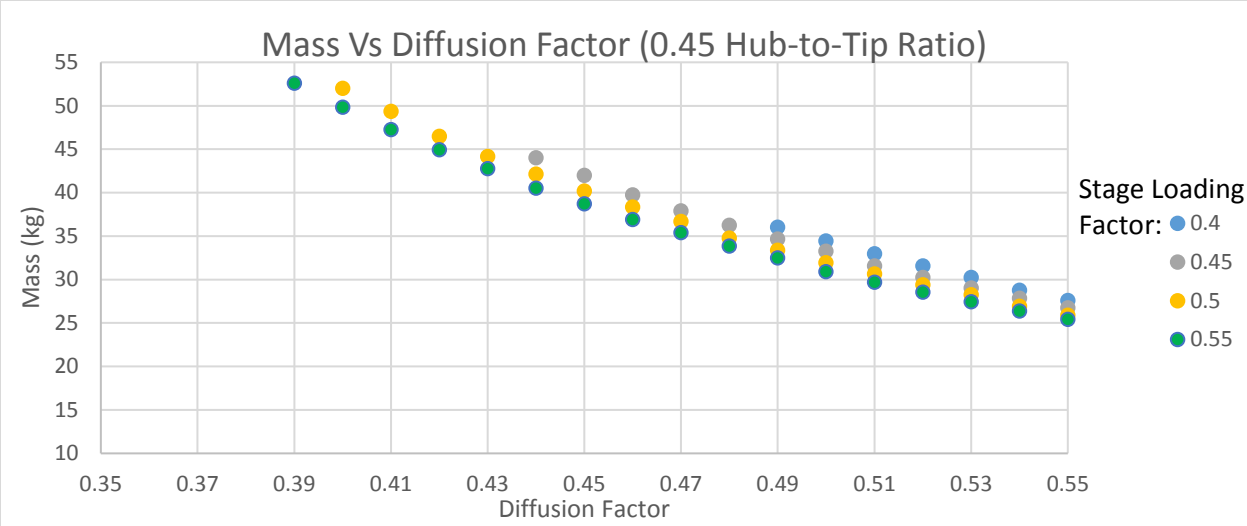

Figure 5 Mass Vs Diffusion Factor for all fan design parametric sweeps.

Hub-to-Tip Ratio had the biggest effect on mass mainly because of how the mass of the disk supporting the bearings was calculated. Blade mass actually increased with reduced Hub-to-Tip Ratio, but the added disk volume canceled out this mass reduction. If a larger bearing OD with a hallow shaft was used for the fan designs with the higher hub to tip ratios this trend may be reversed. Bearing life and efficiency would reduce with the higher bearings surface speeds.

Increasing Diffusion Factor and Stage Loading both decreased fan mass because increasing either parameter reduces the required mass flow. Lower mass flow means less area is needed for all components.

c. Tip Speed

Tip speed is included as the final metric for fan design because it is directly related to motor performance as discussed in the intro. For the motor design explored in this paper higher tip speeds are beneficial until the windage losses become significant. For the motor topology used in this paper windage losses become significant around relatively low tip speeds of .5 to .6 Mach, because of the centripetal pumping created by the rotors. All the fan designs the code produced have tip speeds well below this value so designs with higher tips speeds are always favorable in this case study. The plots in Figure 6 show the tip speeds for all parameter combinations.

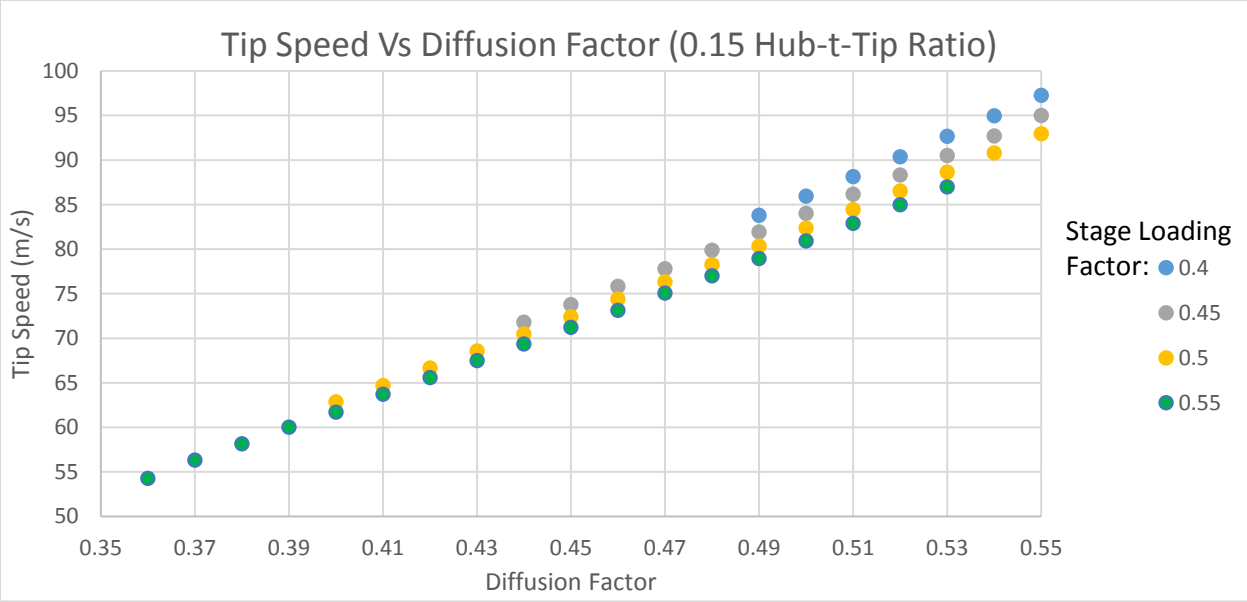

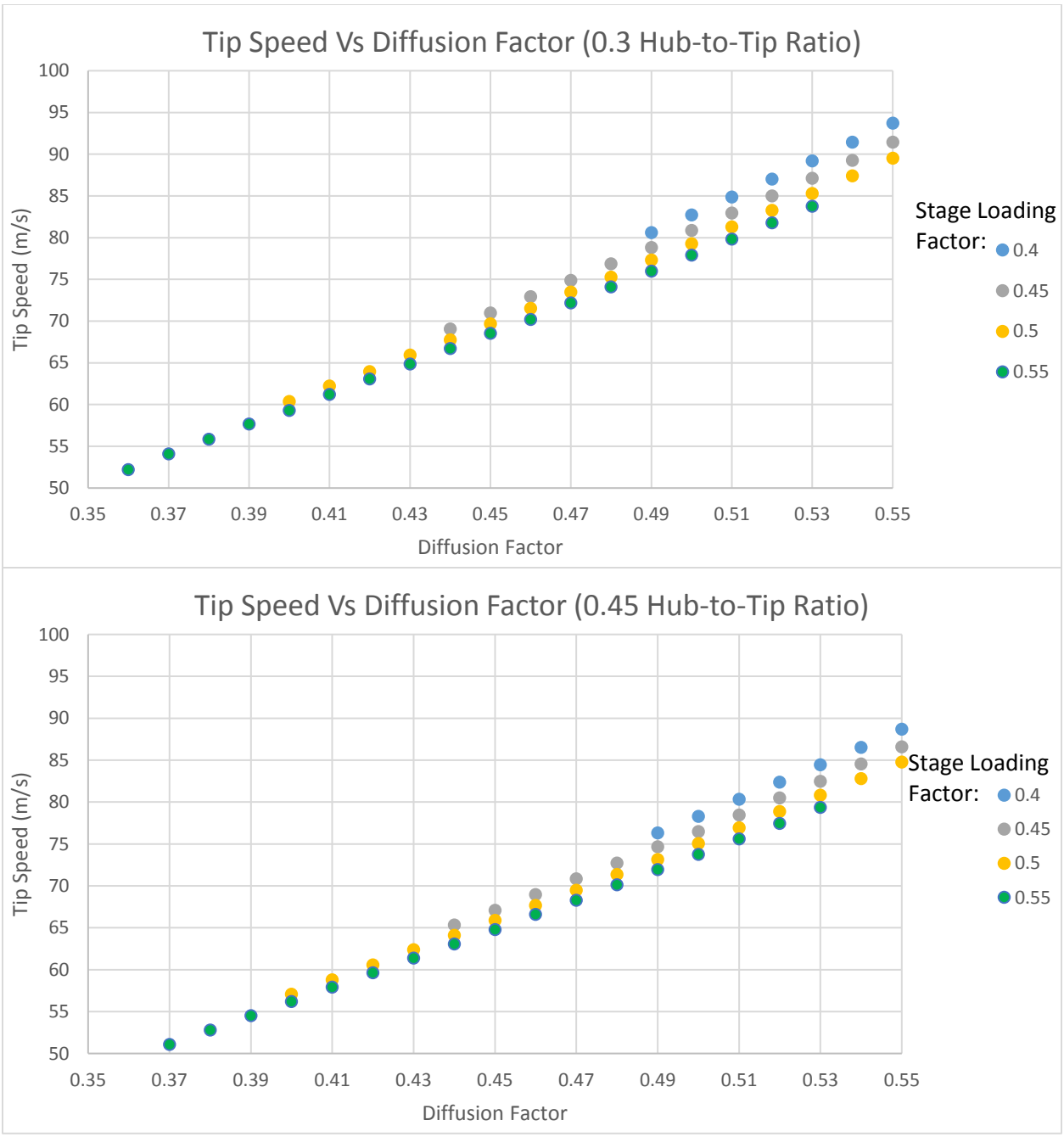

Figure 6 Fan Tip Speed Vs Diffusion Factor

Decreasing Stage Loading increases tip speed as it is directly related to blade mean velocity by equation 16. Diffusion Factor increases tip speed because the coefficient of lift was essentially held constant for a given hub to tip ratio and thereby the only way to achieve high coefficients of pressure is to increase rotational speed. Lowering Hub-to-Tip Ratio increases tip speed because the blades are longer and a larger variation in blade speed results.

2. Fan designs selected for Motor Design

Ten fan designs were selected for motor design in this case study so that the tradeoffs between fan design selection and motor design could be examined. The Table below lists the key metrics for the ten fan designs selected.

Table 4 Selected Fan Designs for Motor Design Code

Design Number	1	2	3	4	5	6	7	8	9	10
Loading Factor	0.4	0.4	0.45	0.45	0.45	0.5	0.5	0.5	0.55	0.55
Hub-to-Tip Ratio	0.3	0.3	0.3	0.3	0.3	0.3	0.3	0.3	0.3	0.3
Diffusion Factor	0.5	0.55	0.45	0.5	0.55	0.41	0.5	0.55	0.37	0.55
Fan Area (m)	0.45	0.36	0.54	0.42	0.34	0.63	0.40	0.32	0.76	0.30
RPM	1986	2525	1559	2008	2542	1265	2030	2561	1004	2578
Tip speed (m/s)	82.71	93.71	70.99	80.86	91.44	62.21	79.29	89.53	54.08	87.84
Tip Diameter(m)	0.80	0.71	0.87	0.77	0.69	0.94	0.75	0.67	1.03	0.65
Hub Diameter (m)	0.24	0.21	0.26	0.23	0.21	0.28	0.22	0.20	0.31	0.20
Mass (Kg)	18.31	14.79	22.39	17.97	14.62	26.63	18.06	14.82	32.21	14.78
Efficiency (%)	79.84%	78.44%	80.71%	79.37%	77.86%	80.79%	79.16%	77.46%	81.18%	76.91%
Power (watts)	53720	54678	53142	54034	55083	53088	54180	55369	52835	55762

Only fan designs with a Hub-to-Tip Ratio of .3 where used, because of concerns about blade crowding at the hub of the .15 Hub-to-Tip Ratio designs and the large masses of the .45 Hub-to-Tip Ratio designs. The goal of the designs selected is to create variation in fan mass, efficiency, and tips speed. All three of these parameters along with tip diameter will have major effects on motor design and the achievable range for X-57.

B. Motor Design Parametric Sweep results

For the motor parametric sweeps the number of stacks and the stack length were varied per the values provided in Table 1. An initial sweep on all ten designs was performed first with a course stack length interval. The results of those sweeps are used to discuss some trends between fan and motor design parameters. Refined sweeps were performed on the highest performing designs in order to arrive at a final design for this case study.

1. Initial sweeps

The initial sweeps were performed with stack lengths in 2.5 mm increments. The resulting optimal motor design and aircraft performance for each fan design used are list in Table 5.

Table 5 Results of Initial Motor Design Code Sweeps for Each Fan Design

Design Number	1	2	3	4	5	6	7	8	9	10
Number of Stacks	1	1	2	2	1	2	2	2	2	2
Active Length (m)	0.0200	0.0200	0.0175	0.0150	0.0225	0.0200	0.0175	0.0150	0.0225	0.0175
Number of Poles	30	23	38	29	23	47	29	23	59	23
Mechanical Mass (kg)	10.58	9.55	11.40	10.17	9.35	12.26	9.98	9.00	13.36	8.79
Motor Power (kW)	54222	55080	53563	54452	55476	53596	54612	56026	53331	56165
Motor Efficiency (%)	97.52	97.54	97.39	97.45	97.50	97.28	97.48	97.52	97.32	97.55
Motor Mass (kg)	12.34	12.10	13.24	12.79	12.29	13.79	12.60	12.22	15.87	12.08
Power Density (kW/kg)	4.39	4.55	4.05	4.26	4.52	3.89	4.34	4.58	3.36	4.65
Total System Mass (kg)	52.34	47.47	58.44	54.19	47.35	64.27	51.83	47.12	73.74	46.68
Aircraft Range (m)	186675	184818	186728	184934	183414	185066	185156	182548	183460	181456

Motor efficiency and mass correlated directly with two parameters: the fan tip speed and the required fan power. The plots in Figure 7 show the trends with respect to tip speed.

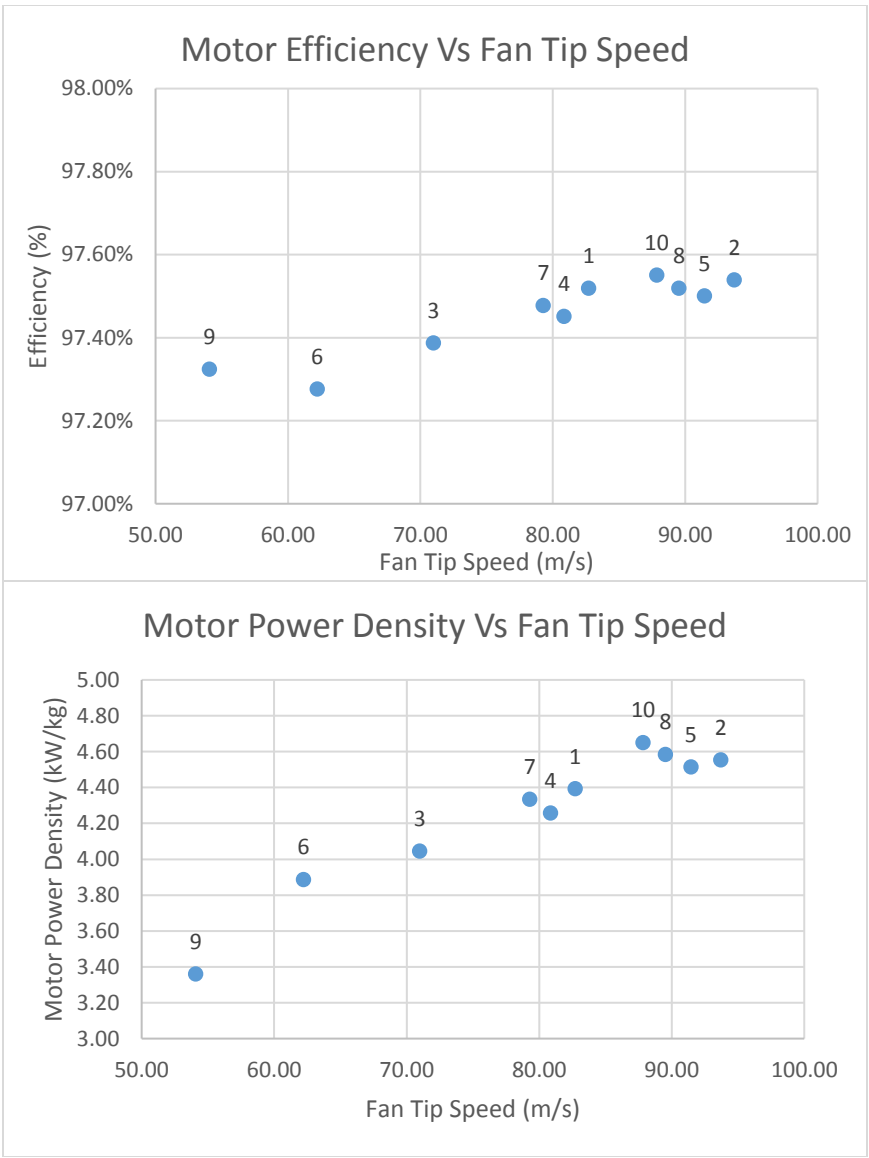

Figure 7 Motor Mass and Efficiency Vs Fan Tip Speed for the 11 Designs

In the tip speed plots a clear relationship between motor performance and fan tip speeds can be seen. As discussed in the intro higher tip speeds lead to lighter more efficient motors.

Tip speed also correlated directly to the number of stacks in the motor design. Generally higher tips speed motors had one stack while lower tips speed motors had two. Low tip speed motors needed larger masses to achieve the required power in one stack. These motors needed to produce more electromagnetic force because of the low tip speeds and thereby required more current. In order to drive more current efficiently they needed a larger mass of copper at longer stack lengths. In one stack, the larger copper mass results in thick stators and large gaps between rotors. The larger gaps between the rotors weakens the field created by a given set of magnets, which in turn also results in higher current requirements or higher magnet thicknesses. Splitting the copper and current over two stacks allows the rotors to stay closer together and drops the required current, copper mass, and magnet mass. The resulting overall design is lighter weight for these low tip speed designs. Additionally, the motor radius goes down limiting the mass of the shell around the propulsor. Splitting the motor into two stacks isn't always beneficial because of the added end windings. In the higher tips speed designs, where the motor can achieve the required power with reasonable stator thicknesses and stack lengths, the added end winding mass outweighs the benefits of two stacks.

Higher fan required power lead to higher mass and more efficient designs. This trend occurs because higher fan required power meant that the fan had both lower mass and lower efficiency. The code therefore balances out the

lower fan mass and efficiency by designing the motor to be more efficient and heavier. The plots in Figure 8 below show these trends.

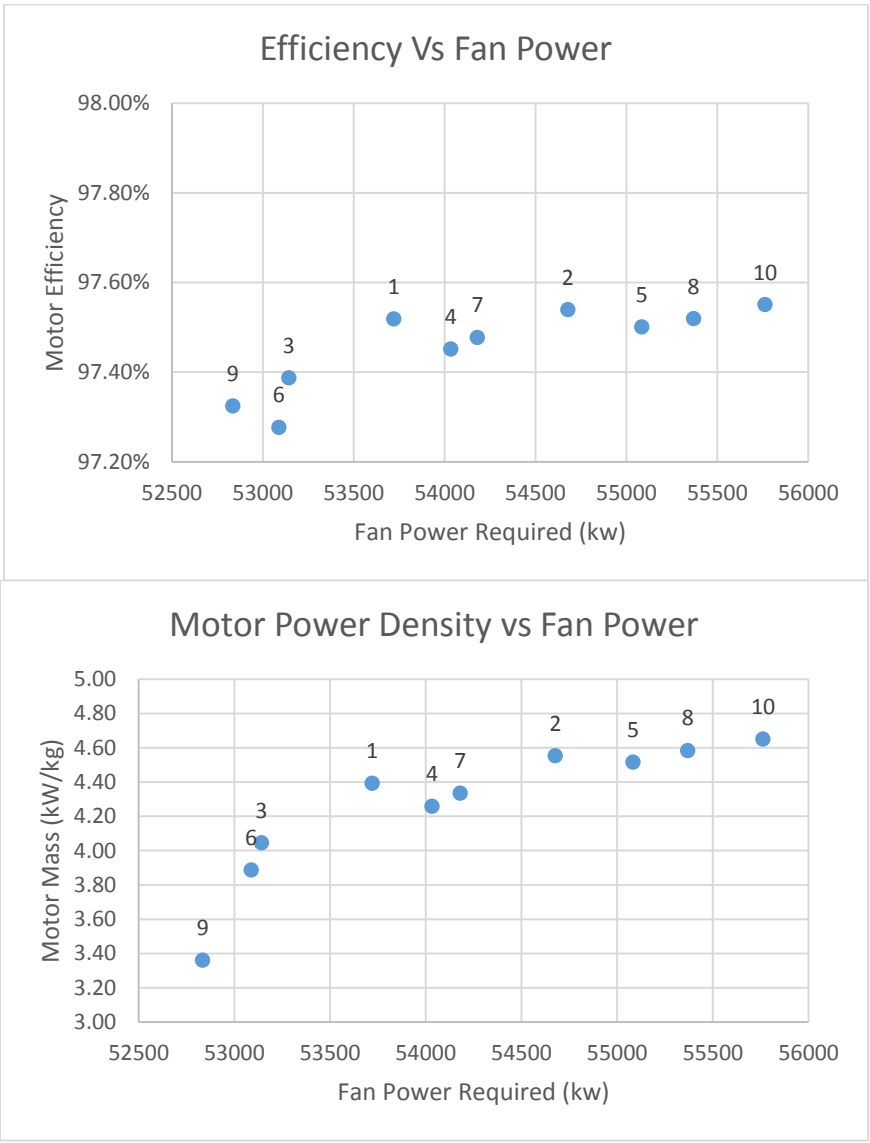

Figure 8 Motor Power Density and Efficiency vs Fan Power for the 11 Designs

The balancing of motor and fan efficiency and mass is how the code optimizes the performance of the overall aircraft. The results of the fan design code show that higher fan efficiency resulted in higher fan mass and lower fan tip speed. Overly high efficiency fan designs therefore result in low motor performance and a heavy overall system. The resulting aircraft performance is low. Design nine is a good example of a very high efficiency fan design and its resulting motor design. Lower fan efficiencies results in low fan mass and high fan tip speed. The resulting motor design has good efficiency and low mass; however, the low fan efficiency results in reduced range. Design eight is a good example of a low efficiency fan design and its resulting motor design.

The designs that achieve the best aircraft performance are the ones that balance the trades between fan efficiency, mass, and tip speed. Designs one and three are good examples of designs that achieve this balance. They have average tip speed, mass, and efficiency relative to the other designs and the resulting motor design has average performance. The resulting propulsion system achieves a good balance between mass and efficiency and aircraft performance improves. Figure 9 shows how aircraft performance varies with fan efficiency.

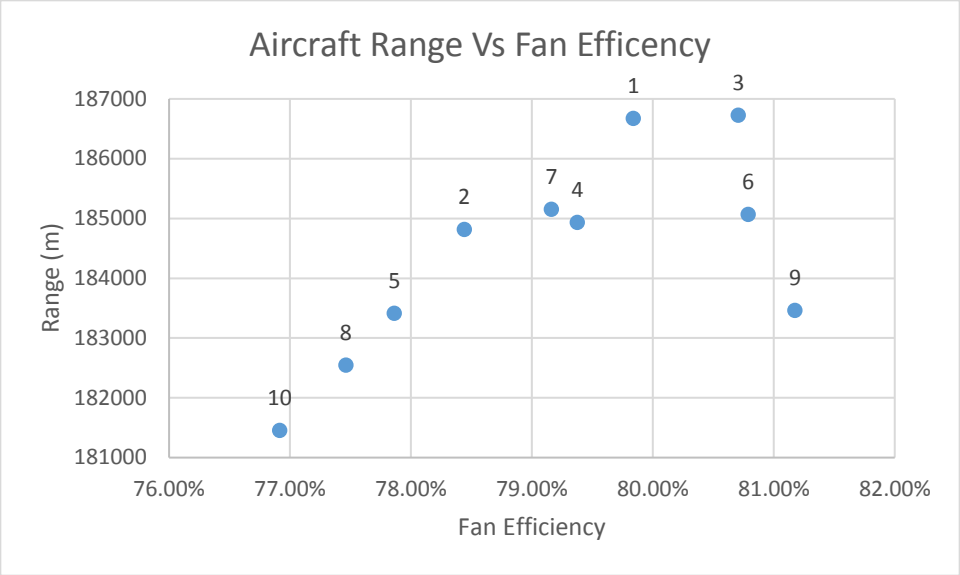

Figure 9 Aircraft Range Vs Fan Efficiency

All designs except for design ten outperformed the baseline design that had an 182300m range. All the designs had lower fan efficiency and higher fan masses than the baseline as would be expected for a ducted fan relative to a prop at these aircraft speeds. The reduced motor mass and improved motor efficiency resulting from the higher motor tip speed however is able to balance out the lower fan performance.

Designs one and three were selected for additional refinement of their motor designs in the following section. An additional design, design 11, that had an efficiency between that of design 1 and design 3 was added based on Figure 9. Table 6 gives its parameters.

Table 6 Design 11 Fan Specifications

Design Number	**11**
Loading Factor	0.45
Hub to tip Ratio	0.3
Diffusion Factor	0.47
Fan Area (m)	0.49
RPM	1731
Tip speed (m/s)	74.89
Tip Diameter(m)	0.83
Hub Diameter (m)	0.25
Fan Mass (Kg)	20.60
Efficiency (%)	80.30%
Power (watts)	53414

2. Refinement of Designs 1, 3, and 11

Designs one, three and eleven where refined by sweeping stack length again with a 0.5 mm increment. The resulting designs are shown in Table 6.

Table 7 Refined Motor Designs for Fan Designs 2 and 5

Design Number	1	3	11
Number of Stacks	1	2	2
Active Length (m)	0.021	0.0165	0.016
Number of Poles	30	38	34
Mechanical Mass (kg)	10.59	11.38	10.90
Motor Power (kW)	54248	53591	53846
Motor Efficiency (%)	97.53	97.38	97.40
Motor Mass (kg)	12.32	13.22	12.96
Power Density (kW/kg)	4.40	4.05	4.16
Total System Mass (kg)	52.33	58.40	55.77
Aircraft Range (m)	186702	186714	186554

Design 3 achieves the highest aircraft performance. Propulsor efficiency is more important than weight for X-57, because the propulsor are a small percentage of the total mass. Design three weighs more than designs one and eleven, but its higher fan efficiency results in better overall aircraft performance.

The results from the study show a potential range increase of roughly 4.4 kilometers for design three over the baseline configuration.

VI. Validation of Feasibility of Proposed Rim Drive Design

A. Thermal Validation

Thermal validation was carried out using an axially symmetric 2D COMSOL combined fluid flow and thermal model. Rough CAD of the nacelle hub and shell was created. The fan was left out of the simulation for simplicity. The nacelle geometry used is not aerodynamically optimized. It was only used to get rough flow fields so that the motor's thermal design could be validated. Geometry for the simulation and results for the model at cruise conditions can be seen in Figure 10.

The motor stator was broken into three sections: one active section and two end turn sections. For the active section the rule of mixtures was used to set its thermal conductivity. The windings in the active section of the motor take up 50% of the available area for design two. The other 50% of the area is assumed to have the same thermal conductivity as the epoxy in the windings 1 (W/(m*K)). The windings are also assumed to be 50% epoxy. The active sections thermal conductivity is therefore estimated as 25% the thermal conductivity of copper plus 75% the conductivity of the epoxy. This estimation results in a thermal conductivity of 97 (W/(m*K)) for the active section.

The end windings' thermal conductivity is modeled using reference 20. In these sections it is assumed that the windings are 50% copper and all the copper is perpendicular to the radial direction. The conductivity is than estimated using

$$k_{end} = k_{epoxy}\frac{\left(k_{epoxy}+k_{epoxy}\right)\left(k_{epoxy}+C_{fill}k_{epoxy}+(1-C_{fill})k_{epoxy}\right)-\delta(1-C_{fill})(k_{epoxy}-k_{epoxy})^2}{\left(k_{epoxy}+k_{epoxy}\right)\left(k_{epoxy}+(1-C_{fill})k_{epoxy}+C_{fill}k_{epoxy}\right)-\delta(1-C_{fill})(k_{epoxy}-k_{epoxy})^2} \quad (28)$$

Here k is thermal conductivity and δ is a constant given by reference 20. For 50% copper fill δ is equal to .835. The resulting thermal conductivity of the end winding sections is 3.24.

Two thermal cases were run based on the mission profile for X-57. The first was cruise conditions. The atmospheric temperatures and air velocity at cruise can be found in Table 2. The losses on the stator at cruise are approximately 1300 watts. The second case was take off. Ambient temperature for this case was set to 313K (40C). Ambient pressure was set to 1atm. Motor power was scaled based on the two powers used for cruise in take off in the original design [Ref. 19]. The two powers differ by 140%. It was assumed that power for design three only scaled through increased current. This way of scaling increases the stator losses to 2600 watts. The air speed for takeoff was set to 35m/s.

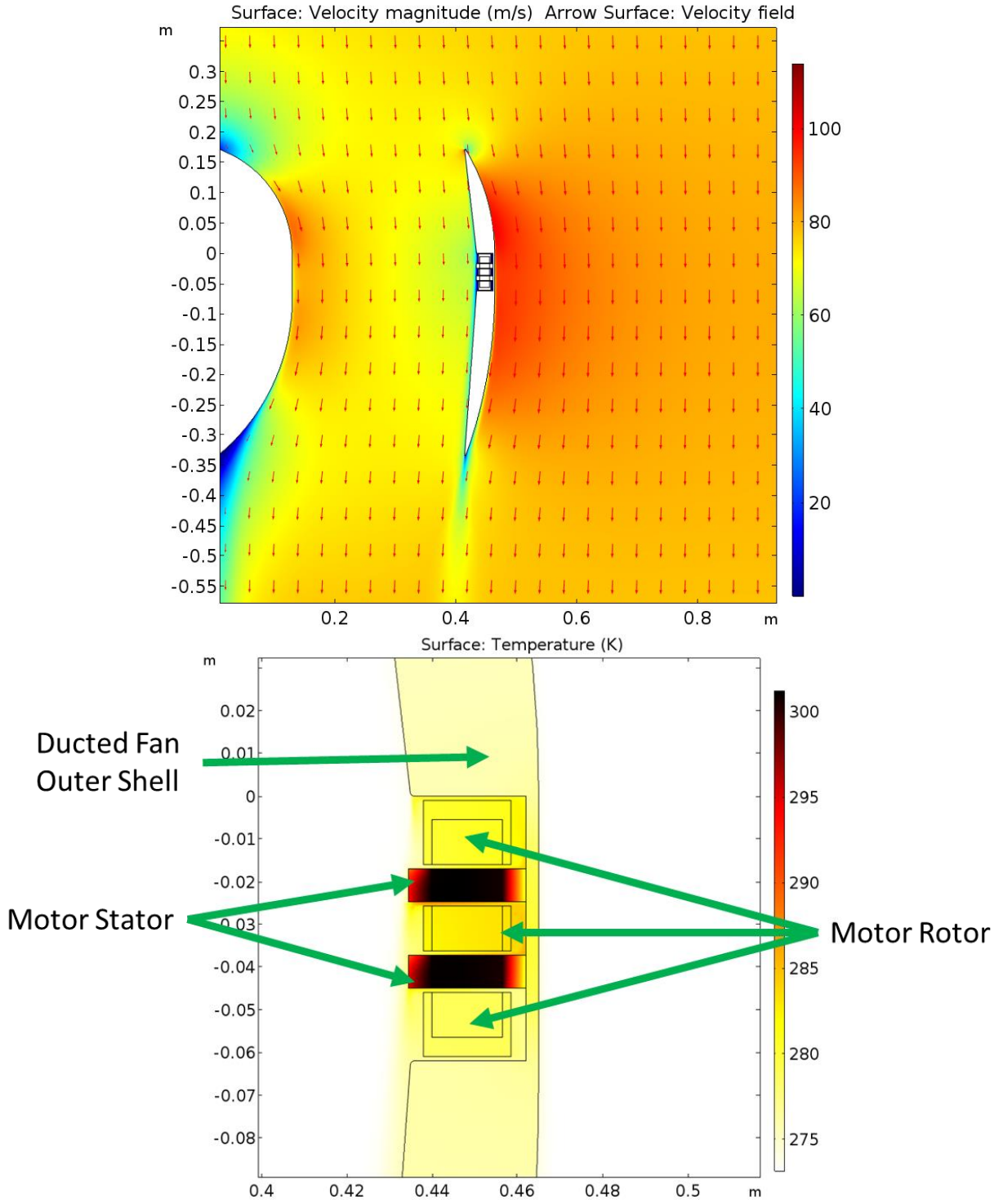

Figure 10 Thermal and Fluid Flow COMSOL Results for Cruise Condition Case

The results for the cruise condition case can be seen in Figure 10. The resulting temperature is 301K. 94 degrees less than the temperature assumed in the motor design. At this temperature copper resistivity would be 75% of what was assumed during the motor design and the motor would be .7% more efficient. The resulting range prediction would be .7% higher.

The results for the takeoff condition case showed a max temperature of 360K; well within the margin available with 420K winding insulation. It should be noted that the 35 m/s is roughly the max take off velocity. The motor will have to be given sufficient thermal inertia to not overheat before X-57 gets to speed. The time to achieve take off velocity is expected to be less than a minute.

B. Electromagnetic Finite Element Analysis

A 2D finite element analysis was carried out in COMSOL to validate the electromagnetic design of the proposed motor design (design three). The simulation was performed at a radial cut plane at the mid radius of the motor. The dimensions in the simulation are defined in the Table 7 below.

Table 8 Design 3 Parameters for 2D FEA Geometry

Simulation Geometry	
Radius	0.4533 (m)
Out of Plane Thickness	0.0165 (m)
Pole Length	0.0749 (m)
Magnet Thickness	0.0105 (m)
Magnet Width	0.082 (m)
Coil Thickness	0.077 (m)
Coil Width	0.0055 (m)
Rotor Phase Offset	75 (degrees)
RMS Current	313 (A)

All the dimensions, currents, and the load angle were defined by the motor design code. The out of plane thickness of the simulation was set equal to the motor stack length. Only the two outer rotors where halbach arrays. The middle rotor was modeled with a normal north south magnet array. Two pole pairs were simulated, but electromagnetic force was only calculated using a single pole to eliminate the possibility of boundary conditions affecting the results. The force was evaluated at the coils only in the x direction. This force was turned into a torque estimate by multiplying by the number of poles in design three and the radius of the simulation cut plane. The magnetic field results from the simulation can be seen in Figure 11 below.

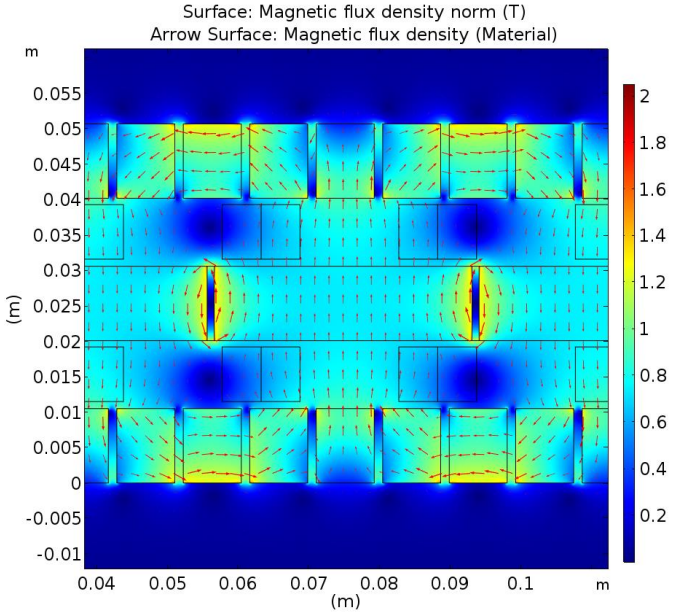

Figure 11 One Pole Pair of the Electromagnetic Simulation Results.

The design code predicted 330 Nm of torque for the full motor. The COMSOL FEA simulation predicted 310 Nm. The design code over predicted the torque by 6%. This level of error is expected with the low fidelity motor model used.

To correct the design, the motor design code was rerun with a correction factor that adjusted the codes predicted torque by 6%. The resulting motor performance is summarized in Table 9 below.

Table 9 Updated Motor Design Code Results with Correction Factor for Fan Design 3

Design Number	2
Fan Tip Speed (m/s_	80.90
Fan Mass (Kg)	15.91
Fan Efficiency (%)	89.89%
Active Length (m)	0.0165
Number of Poles	38.00
Mechanical Mass (kg)	11.38
Motor Power (kW)	53524
Motor Efficiency (%)	97.32%
Motor Mass (kg)	14.18
Total System Mass (kg)	59.68
Aircraft Range (m)	186251

The resulting update motor configuration reduces the range by 463 meters. The changes to the motor are the same as those that would result from an increase in required fan power, because the correction factor essentially increased the required power the code was asked for by 6%. Mass increases and efficiency decreases slightly.

The COMSOL model was updated with the updated motor design geometry. The design code still predicts 330 Nm of torque because the required torque for the fan was not changed. The COMSOL model predicted 325 Nm of torque for the updated geometry. The resulting percent error between the two simulations is now 1.5%

C. Bearing Design

As an initial step in the mechanical design of the motor bearing analysis was completed to layout the support structure for the rotor. The analysis showed that the assumed bearing may be too small depending on the dynamic loads in high pitch and yaw maneuvers.

The bearing analysis was carried out using the method recommended in the SKF catalog [Ref 9]. First, the mass of the rotor structure was determined M. This was necessary to calculate the radial load F_r, which was the weight of the rotor in kN. Mass was also needed for the later calculation of the fan inertia term. The axial load on the bearing F_a was set equal to the fan thrust at cruise in kN. For the bearing type assumed in the motor design the appropriate calculation factors are shown in Table 10.

Table 10 Bearing Calculation Factors

Calculation Factor	Value
e	0.80
X	0.63
Y1	0.78
Y2	1.24
Y0	0.66

These factors were used to calculate equivalent dynamic bearing load P in kN. Equivalent dynamic bearing load was determined by the equality:

$$\frac{F_a}{F_r} \leq e \ \rightarrow P = \ F_r + \ Y_1 * F_a \tag{29}$$

$$\frac{F_a}{F_r} > e \ \rightarrow P = \ X * F_r + \ Y_2 * F_a \tag{30}$$

A simplified frictional moment model was used to determine bearing losses, one assumption for which was that the equivalent bearing dynamic load was approximately one tenth the basic dynamic load rating C.

$$C = {}^{P}/_{0.1} \tag{31}$$

The power loss for the bearings could then be determined using equation 9
The flight hours of the bearing were determined by:

$$L_{10h} = \frac{10^6}{60 * n}\left(\frac{C}{P}\right)^p \tag{32}$$

With n equal to the rpms and p equal to 3 for ball bearings.

The radial loads generated by the rotor while performing a high G maneuver was also resolved to ensure that moments generated in this case did not overload the rotor bearing. It was assumed that the maximum yaw or pitch speeds in the maneuver n_m were both 2 rad/s. The inertia of the rotor was modeled as a solid disk so that the inertia about the rotational axis was:

$$I_z = \frac{1}{2} * M * R^2 \tag{33}$$

And the inertia about the pitch and yaw axis was:

$$I_x = I_y = \frac{1}{4} * M * R^2 \tag{24}$$

The resulting gyroscopic moment vector is:

$$M_G = \ I_z * n * \left({}^{2 * \pi}/_{60}\right) * n_m \tag{35}$$

This results in an additional radial load equivalent to the gyroscopic moment divided by the force reaction location distance from the moment center of the double row bearing a. The radial load was recalculated as:

$$F_r = \ \left(\left(F_g + {}^{M_G}/_{a}\right)^2 + \left({}^{M_G}/_{a}\right)^2\right)^{1/2} \tag{36}$$

Where F_g was the weight of the rotor and M_G was used twice with the assumption that the 2 rad/s pitch and yaw maneuvers were performed simultaneously. The previous equations for calculating equivalent dynamic bearing load P were used to ensure that in this loading scenario the new P did not exceed C_{sel}.

The life analysis showed that the assumed bearing could survive 600,000 hours but did not have sufficient dynamic load carrying capacity for the worst case gyroscopic loads. The max allowable lifetime is at least an order of magnitude higher than what would be required. The estimated losses form this bearing was 4 Watts. A bearing with a 45mm bore diameter of the same class would be able to withstand the worst case dynamic loads. It would be .2kg heavier, have 2 watts more of losses, and have a reduced life of 200,000 hours. The larger bearing may however allow for a reduction in fan hub mass and a more stable shaft design.

VII. Conclusion

In this paper, a proof of concept version of an electric propulsion system design code is presented. The code uses low fidelity aircraft, fan, and motor models to develop a propulsion system that maximizes the range of a given aircraft. A case study using X-57 as the aircraft is used to demonstrate the code.

The version of the code presented here is for an axial flux dual rotor air core rim driven propulsor. Rim driven fans allow motors to operate at closer to their optimal tip speed. Air core machines enable high electrical frequencies and high motor tip speeds to be used without frequency dependent losses associated with iron cores. The case study in this paper shows a potential 4 kilometer improvement in X-57's range if this propulsion system topology is used. Some higher fidelity validation of this design is presents. The accuracy of this result needs to be validated further. Unfortunately it is not possible to decouple the benefits of the propulsion system topology change from the benefits of the design methodology used. The methodology would have to be applied to a radial hub driven fan for a more direct comparison to the baseline topology to truly determine if it is beneficial.

Continued development of this code will focus on refining its accuracy and making it more versatile. The next steps for continued code development are

1. Adding a propeller model so hub driven fans can be designed
2. Improving coupling of fan and motor design
3. Additional stress analysis calculation and higher fidelity mass estimate.

4. Higher fidelity thermal models that predict motor temp at each mission segment
5. Inclusion of nacelle drag calculations.
6. Enabling the code to account for the more complicated mission profiles that would exist for vertical takeoff and landing vehicles.
7. Developing a low fidelity gear box design model to allow for the design of geared motors
8. Developing motor design codes for high speed radial flux machines
9. Integrating the electric propulsion system design code with aircraft design code so that a metric other than max aircraft range can be targeted

Acknowledgments

The authors would like to thank the NASA Convergent Aeronautic Solutions (CAS) project for pre-work and incubation funding.

References

[1] Arkkion, A., Jokinen, T., and Lantto, E., "Induction and Permanent-Magnet Synchronous Machines for High-Speed Applications," Proceedings of 8th International Conference on Electrical Machines and Systems, IEEE, 2005

[2] Patterson, M.D., German, B.J., and Moore, M.D., "Performance Analysis and Design of On-Demand Electric Aircraft Concepts," 12th AIAA Aviation Technology, Integration, and Operations Conference, AIAA, Indianapolis 2012

[3] Duffy, K., "Optimizing Power Density and Efficiency of a Double-Halbach Array Permanent-Magnet Ironless Axial-Flux Motor," 52nd Annual AIAA/SAE/ASEE Joint Propulsion Conference, AIAA, Salt Lake City, 2016

[4] Halbach, K., "Application of permanent magnets in accelerators and electron storage rings," J. Appl. Phys. 57, 3605, 1985.

[5] Gieras, J. F., Wang, R. J., and Kamper, M. J., *Axial Flux Permanent Magnet Brushless Machines*, Springer, 2008.

[6] J. Saari, "Thermal analysis of high-speed induction machines," Ph.D. Dissertation, Dept. Elect. Commun. Eng., Helsinki Univ. Technol., Espoo, 1998.

[7] Z. Huang, J. Fang, X. Liu, and B. Han, "Loss calculation and thermal analysis of rotors supported by active magnetic bearings for high speed permanent-magnet electrical machines," IEEE Trans. Ind. Electron., vol. 63, no. 4, Apr. 2016, pg. 2027–2035,

[8] A. Krings, "Iron Losses in electrical Machines – Influence of Material Properties, Manufacturing Processes, and Inverter Operation" Doctoral Thesis KTH University. Stockholm, Sweden 2014

[9] SKF Group, "SKF Rolling Bearings Catalogue," August, 2016. http://www.skf.com/binary/77-121486/SKF-rolling-bearings-catalogue.pdf,

[10] Incropera, F. and DeWitt, D., *Fundamentals of heat and mass transfer*, J. Wiley, 2002.

[11] Dixon, S. L., and Hall, C. A., *Fluid Mechanics and Thermodynamics of Turbomachinery*, 7nd ed., Elsevier Inc., Waltham, 2014, Chap. 5.

[12] Farokhi, Saeed, *Aircraft Propulsion*, John Wiley and Sons Inc., Danvers, 2009, Chap. 4, 5, 7.

[13] Howell, A. M., "Fluid Dynamics of Axial Compressors," *Proceedings of the Institution of Mechanical Engineers*, Vol. 153, 1945, pp. 441–452

[14] Turner, R.C., "Notes on Ducted Fan Design," Ministry of Aviation C.P. No 895, 1964.

[15] Pera, R. J., Onat, E., Kleees, G.W., and Tjonneland E., "A Method to Estimate Weight and Dimensions of Aircraft Gas Turbine Engines," NASA Report Cr135170, 1977.

[16] NASA Armstrong Flight Research Center, *NASA X-57 Critical Design Review*, Palmdale, CA. Nov 15, 2016. https://www.nasa.gov/X-57/technical/index.html, Day 1&2 Package

[17] Deere, K., Viken, J., Viken, S, Carter, M., Wiese, M., Farr, N., "Computational Analysis of a Wing Designed for the X-57 Distributed Electric Propulsion Aircraft", AIAA Aviation Forum 2017, Denver CO, June 5-9, 2017

[18] Borer, N. K., Patterson, M. D., Viken, J. K., Moore, M. D., Bevirt, J., Stoll, A. M., and Gibson, A. R., "Design and Performance of the NASA SCEPTOR Distributed Electric Propulsion Flight Demonstrator," 16th AIAA Aviation Technology, Integration, and Operations Conference, AIAA, 2016.

[19] Dubois, A., van der Geest, M., Bevirt, J., Christie, R., Borer, N. K., and Clarke, S. C., "Design of an Electric Propulsion System for SCEPTOR's Outboard Nacelle," 16th AIAA Aviation Technology, Integration, and Operations Conference, AIAA, 2016.

[20] Popescu, M., Dorrell, D.G., Alberti, L., Bianchi, N., Staton, D.A., and Hawkins D., "Thermal Analysis of Duplex 3-Phase Induction Motor Under Fault Operating Conditions," IEEE Transactions on Industrial Applications, IEEE, 2013.